# On Fault Diagnosis for High-g Accelerometers via Data-Driven Models

Jingjing Wen, Houpu Yao, Ze Ji, *Member*, *IEEE*, Bin Wu, and Min Xia, *Member*, *IEEE*

***Abstract*—Shock test is a pivotal stage for designing and manufacturing space instruments. As the essential components in shock test systems to measure shock signals accurately, high-g accelerometers are usually exposed to hazardous shock environment and could be subjected to various damages. Owing to that these damages to the accelerometers could result in erroneous measurements which would further lead to shock test failures, accurately diagnosing the fault type of each high-g accelerometer can be vital to ensure the reliability of the shock test experiments. Additionally, in practice, an accelerometer in one malfunction form usually outputs mutable signal waveforms, so that it is difficult to empirically judge the fault type of the accelerometer based on the erroneous readings. Moreover, traditional hardware diagnosis approaches require disassembling the sensor's package shell and manually observing the damage of the elements inner the sensor, which are less efficient and uneconomical. Aiming at these problems, several data-driven approaches are incorporated to diagnose the fault types of high-g accelerometers in this work. Firstly, several high-g accelerometers with most frequent types of damage are collected, and a shock signal dataset is gathered by conducting shock tests on these faulty accelerometers. Then, the obtained dataset is used to train several base classifiers to identify the fault types in a supervised fashion. Lastly, a hybrid ensemble learning model is established by integrating these base classifiers with both heterogeneous and homogeneous models. Experimental results show that these data-driven methods can accurately identify the fault types of high-g accelerometers from their mutable erroneous readings.**

***Index Terms*—shock test, high-g accelerometer, fault diagnosis, data-driven methods, ensemble learning.**

## I. Introduction

IN aircraft/aerospace engineering, the on-board electronic instruments would undergo multifarious high-g shock environments [1], such as the release of space equipment with explosive bolts [2], the impact of orbital debris on spacecraft structures [3], and the bird striking [4]. With aim to verify if the space instruments could withstand the severe shock loads structurally and functionally, various ground shock test standards have been developed by standardization bodies, e.g. ISO, JEDEC, IEC, etc., to simulate the real shock environments, and passing the shock test is an essential requirement during designing and manufacturing space instruments [5].

Shock environments are described by acceleration-time signals generally, which can be measured by accelerometers [6]. However, high-g accelerometers sometimes can get damaged during the shock tests due to the severe impact environment [7]. These damaged accelerometers cannot measure accurate shock signals, which would lead to measuring uncertainties of various unpredictable levels, and, hence, test failures. Additionally, using uncalibrated accelerometers, but without awareness beforehand, would result in the test failure as well [8]. There are mainly two categories of accelerometer faults: the damage of the package shell and the damage of the inner components [9]. While the package shell damage can be diagnosed visually, inner components damage cannot be observed directly. Accordingly, this work primarily addresses the identification of the inner components damage. The major damage types of accelerometer's inner components include cantilever fractures, wire bond shearing, solder joint loss, chip cracks, [10], [11] etc. Correspondingly, inner component damages will cause the waveform variation of the accelerometer's outputs, such as the peak truncation [7], noise pollution [8], and baseline drift [12]. Therefore, it would be of great value to be able to automatically diagnose the accelerometer's fault type through its readings.

Currently, identifying the fault type of accelerometers heavily relies on human estimation and prior experience in signal processing [13], [14]. Such a dependency on human ingenuity limits the extension for more complicated scenarios [15]. Additionally, the output signals of a faulty accelerometer sometimes lack repeatability, and, thus, the sensors with different fault types are likely to output similar signal waveforms, which further increases the difficulty of diagnosing accelerometers' fault types through their output readings. Over the past decade, data-driven methods have achieved great success in the fault diagnosis field based on its strong feature extraction ability and high performance in approximating complex functions [16]. Typical fault diagnosis applications are developed in the fields of rotary machinery systems [17], battery systems [18], and engineering structures [19]. All the works not only enrich the applications of the data-driven methods but also improve the fault diagnosis level in these fields. However, to the authors' best knowledge, research in automating fault identification on shock sensors is still limited, and, hence, the authors are motivated to investigate in methods for automatic inference of fault types of accelerometers by directly analyzing their outputting readings.

Manuscript submitted April 13, 2020. This work was supported by the Innovation Foundation for Doctor Dissertation of Northwestern Polytechnical University (No. CX201902). (*Corresponding author: Ze Ji; Min Xia.*)

J. Wen is with the School of Astronautics, Northwestern Polytechnical University, Xi'an, Shaanxi 710072, China, and also with the School of Engineering, Cardiff University, Cardiff CF243AA, U.K. (e-mail: wjj1990@mail.nwpu.edu.cn).

H. Yao is with the JD Finance America Corporation, Mountain View, CA 94043, USA (e-mail: hope-yao@asu.edu).

Z. Ji is with the School of Engineering, Cardiff University, Cardiff CF243AA, U.K. (e-mail: jiz1@cardiff.ac.uk).

B. Wu is with the School of Astronautics, Northwestern Polytechnical University, Xi'an, Shaanxi 710072, China (e-mail: wubin@nwpu.edu.cn).

M. Xia is with the Yangtze River Delta Research Institute, Northwestern Polytechnical University, Taicang, Jiangsu 215400, China (e-mail: mxia87@gmail.com).

In this work, firstly, a dataset of shock signals from shock tests are generated by using a high-g shock testing system. This shock testing system is composed of a drop shock tester [5] and a dual mass shock amplifier (DMSA) [20], which is capable of producing high-g shock signals on the order of $1\times 10^4$ g and conducting shock tests with high efficiency. The gathered dataset contains 3004 sets of shock signals measured from one healthy accelerometer and six faulty accelerometers. For most traditional data driven-based fault diagnosis methods, all the training datasets and label information are simulated from laboratory machines, which could not be representative enough for real-life operating conditions [21]. In this work, all the faulty types of accelerometers and all the data are gathered from real-world experiments. Secondly, five main-stream data-driven models have been investigated; benchmarked on the collected dataset to detect different types of sensor faults. The models used in this paper include multiple-hidden-layer neural networks (MHLNN), logistic regression (LR), *k*-nearest neighbor (*k*-NN), support vector machine (SVM), and ensemble learning (EL). Among these models, the Bagging algorithm is employed to construct the EL model by integrating the other four models, which are set as the base classifiers. Lastly, the diagnosis results of the proposed data-driven methods are visualized and evaluated with several metrics, including confusion matrix, accuracy, precision, recall, $F_1$-score and computation time. The tested results show that the proposed data-driven-based diagnosis methods can effectively identify fault types from mutable shock waveforms. Especially, the EL model demonstrates superior identification performance to the other four single data-driven models.

The major contributions of this work are highlighted below:

(1) To the authors' best knowledge, this is the first time to introduce data-driven methods into fault diagnosis of high-g accelerometers, hence contributing a new application for machine learning methods.

(2) A new dataset for industrial shock signals is established. This dataset contains several typical fault types of shock sensors and are gathered from real engineering practice, which will facilitate future research for both fault diagnosis of high-g accelerometers and signal measurement in shock tests.

(3) A hybrid EL framework is explored for the fault diagnosis problem of high-g accelerometers for the first time by integrating both heterogeneous and homogeneous models, featuring high accuracy and generalization.

## II. Preliminaries of Related Data-driven Methods

The aim of this work is concentrated in learning from labeled shock signals and predicting the damage type of accelerometers when a new signal is given. This type of task falls into the supervised learning category. In this section, five popular supervised learning methods used in experiments are reviewed briefly, including MHLNN, LR, *k*-NN, SVM, and EL. Without loss of generality, the basic binary classification problem is used to illustrate the algorithms for the sake of simplicity. The details of these methods can be referred in [22].

Neural network (NN) can be viewed as a parametric function $f(\boldsymbol{x}|\boldsymbol{w}) = h^{\mathrm{L}}(w^{\mathrm{L}}, \dots, h^2(w^2, h^1(w^1, \boldsymbol{x})))$ with parameters $\mathrm{w}^l(l = 1,2, \dots, \mathrm{L})$ for each layer and the network input $\boldsymbol{x}$. $h^l(l = 1,2, \dots, \mathrm{L})$ is named as activation function, which is usually chosen as the ReLU function [23]. The single hidden layer NN is easy to train and has been widely used, but its shallow structure limits the ability to further mine fault information and identify fault types. A typical deep learning model is MHLNN, which enhances the capacity of the model by increasing the hidden layers. It has been proven that, given enough weights, the NN is able to approximate any complex function. In the training phase, the optimum weights $\boldsymbol{w}^*$can be determined by minimizing the difference between the NN output and the observations ($\boldsymbol{y}$), i.e. $\boldsymbol{w}^* = \arg\min(f(\boldsymbol{x}|\boldsymbol{w}), \boldsymbol{y})$, and such optimization problems can be solved efficiently with the error back-propagation algorithm.

The LR algorithm is obtained by applying the sigmoid function and maximum likelihood method to the output of LR, i.e., $L(\boldsymbol{\beta}) = \sum_{i=1}^{m}(\ln(1 + \mathrm{e}^{\boldsymbol{\beta}^T\widehat{\boldsymbol{x}}_i}) - y_i\boldsymbol{\beta}^T\widehat{\boldsymbol{x}}_i)$, where $\widehat{\boldsymbol{x}}_i = (\boldsymbol{x}; 1)$ $(i = 1,2, \dots, m)$ is the input data; $\boldsymbol{\beta} = (\boldsymbol{w}; b)$ are the weight parameters; $y_i$ is the label. In the training phase, the optimum weights $\boldsymbol{\beta}^*$can be determined by minimizing $L(\boldsymbol{\beta})$, i.e. $\boldsymbol{\beta}^* = \arg\min L(\boldsymbol{\beta})$, and such optimization problems can be solved effectively with the convex optimization theory. The sigmoid function is shown in Fig. 1.

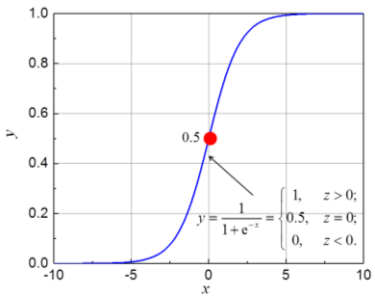


Fig. 1. Illustration of the sigmoid function.

The *k*-NN algorithm is based on a simple assumption that similar things are near to each other. A variety of distance measurements has been proposed to identify the neighborhood, such as the Euclidian distance, Mahalanobis distance, and Bhattacharyya distance. In practice, given a testing data point, the nearest neighbor to it can be found in the training set and the most frequent label is regarded as the label to the testing data. An illustration of the Euclidian distance-based *k*-NN algorithm with *k*=3 is shown in Fig. 2. An advantage of *k*-NN is that it requires few training parameters for implementing, which greatly simplifies the computation of this algorithm.

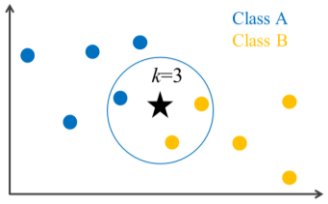


Fig. 2. Illustration of *k*-NN algorithm with *k*=3.

The SVM method is an elegant algorithm and has achieved great success since the 1990s. As shown in Fig. 3, the idea of SVM is to find a hyper-plane in the high dimensional feature space that distinctly classifies the training data. Data falls into different sides of the hyper-plane is regarded as different classes. A nice convex optimization problem can be formulated under such a problem setup to find the support

vectors, allowing fast solution and easy error estimation. Different kernel functions have been introduced to extend this algorithm, making SVM handle nonlinear separable cases well [24].

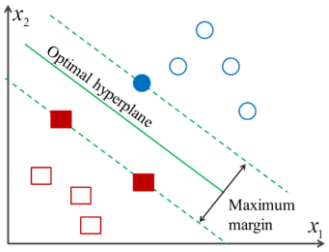


Fig. 3. Illustration of the SVM method (different colors represent different classes; the filled squares and circles correspond to the support vectors of the dataset).

As shown in Fig. 4, EL is a machine learning approach which can obtain better classification accuracy and generalization by combining multiple base classifiers. Generally, the base classifiers are simple with little computation, and the diversities among these base classifiers are the primary requirement instead of the classification accuracy [25]. Theoretically, the classification performance of the integrated classifier trained with EL is better than that of each stand-alone base classifier [25]. Base classifiers can be of the same type or different types, termed as homogeneous ensemble models and heterogeneous ensemble models respectively [26]. According to the strength of the dependencies between the base classifiers, EL method can be roughly divided into two categories: serial and parallel generation methods. The former adapts to the condition that there are strong dependencies between the base classifiers, and the representative strategy is the Boosting algorithm. Oppositely, the latter applies to the situation that there are weak dependencies between base classifiers, and the typical approach is the Bagging algorithm. In the last few decades, EL methods have been successfully employed for the fault diagnosis in various fields, including rotary machineries [25], gas turbine engines [26], photovoltaic systems [27], etc.

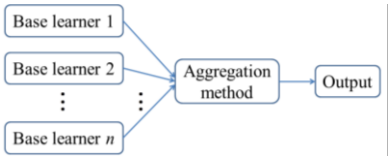


Fig. 4. Schematic diagram of EL method.

## III. Experimental System and Data Collection

In many previous studies for fault diagnosis, fault types are simulated using laboratory machines in some predefined conditions to mimic the fault behaviors [17], [28]. Lei and Lu *et al*. point out that the fault diagnosis knowledge from laboratory machines is different from real-case machines [21], [29]. In this work, all the tested accelerometers are collected from actual practice, and the experimental system is a standard shock test setup which can produce real shock test environments.

Fig. 5 displays the high-g shock test system used in this work to generate the dataset and verify the performance of the proposed data-driven methods. This system combines a drop shock tester [5] and a DMSA [20]. The working principle of this platform is as follows: Firstly, lift the drop table and the DMSA up to a drop height and then release them in free fall together; Secondly, a strong collision will occur with the drop table falling on the rubber programmer producing a primary impact, and bounce upward due to the programmer's elasticity; Lastly, the DMSA table will continue moving downward and collide with the upward-moving DMSA base in a secondary impact, producing a high-g shock. In this system, different drop heights will generate different shock levels, and a dataset containing massive shock signals with different shock levels can be obtained by repeating these procedures. This system can be used as a standard device for high-g shock tests directly, and, thus, the collected dataset is highly consistent with the practical working conditions of real shock test.

In this work, one functional accelerometer and six faulty accelerometers, which were all collected from practical shock tests, are used to measure shock signals simultaneously. As shown in Fig. 5, these accelerometers are connected to the charge amplifier with signal lines. After amplification, the shock signals are transmitted into the data acquisition and processing system through a shielded signal cable. The sampling frequency is 200 kHz, which guarantees the high fidelity of the measurements. Then the processed shock signals can be visualized on the monitor directly.

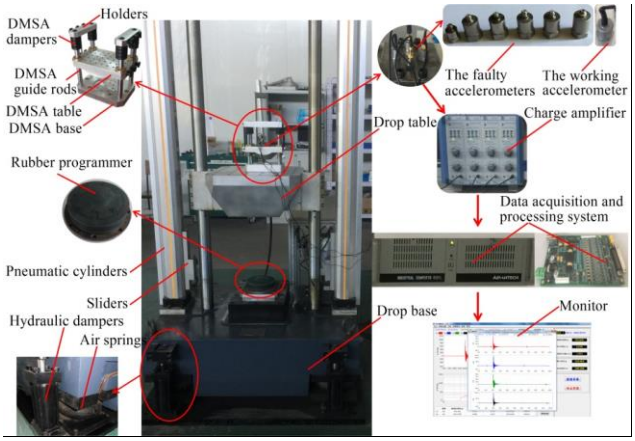


Fig. 5. Experimental system. More details can be found in [7].

Besides, in order to eliminate the incommensurability between different types of sensors, the used accelerometers are all the piezoelectric type. As shown in Fig. 6, the piezoelectric accelerometer is generally composed of the shell, a mass block, a piezoelectric element, and so on. The working principle is introduced briefly here. The base of the accelerometer is fixed on an object rigidly with the mounting bolt, and move at the same acceleration with the object. When conducting measurement, the piezoelectric element is subjected to the inertial force of the mass block opposite to the acceleration direction, and an alternating charge is generated on both surfaces of the piezoelectric element. After amplification, the value of the charge can be measured by the measuring instrument, and the acceleration of the object is obtained [30].

In this work, a total of 751 times shock tests with different drop heights were conducted and 3004 sets of shock signals were collected. In order to acquire the shock information as accurate as possible, no pre-processing was carried out on these signals. The typical readings from all the accelerometers under different fault types are displayed in Fig. 7. These typical signal readings were picked out manually and empirically. It can be seen from Fig. 7 that, except accelerometers 1 and 3, every other faulty

accelerometer with one fault type demonstrates mutable faulty signal waveforms, and different faulty sensors could output similar faulty waveforms too. The detailed description for the faulty readings of each accelerometer is summarized in Table I. Therefore, it is considered highly challenging to be able to accurately identify the fault type of the accelerometer from its erroneous readings empirically. This phenomenon that sensors with different fault types output similar readings could be caused by the low repeatability of the faulty sensors. Besides, it is worth noting that these erroneous shock waveforms are measured from the accelerometers used in this work, but in practice, even with the same fault type, different signal waveforms can be produced under different experimental environments and different sensor types.

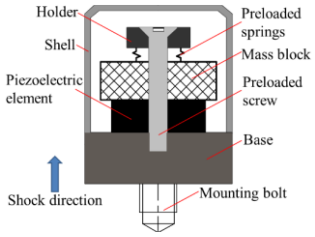


Fig. 6. Schematic diagram of piezoelectric accelerometer's structure.

## IV. Training and Testing of the Data-driven Methods

### A. Training and Testing of the Base Classifiers

In the gathered 3004 sets of shock signals, 80% of the samples for each accelerometer were randomly extracted as the training dataset, and the remaining 20% were maintained as the test dataset. Four different models, including MHLNN, *k*-NN, LR, and SVM, are trained on the dataset, and the fault types of these accelerometers are monitored by classification.

The MHLNN used in this paper has three hidden layers, with 512, 32 and 8 nodes respectively. The MHLNN is trained for 200 epochs, and the training process for the proposed MHLNN is monitored in Fig. 8. The Adam optimizer with a learning rate of $1 \times 10^{-4}$ and batch size of 32 was used. It can be seen that both training and testing accuracy are converging well.

The number of neighbors used in the *k*-NN algorithm is evaluated with values ranging from 2 to 9. The testing accuracy for the *k*-NN models with different numbers of neighbor is monitored to indicate the performance of the corresponding *k* values. As shown in Fig. 9, the accuracy first increases and then decreases with the increasing neighbors. This is due to that the model is over-fitting with smaller *k* and tends to be under-fitting with larger *k*. Besides, it can be seen that the *k*-NN model gets the optimal accuracy when *k* equals to 3.

The gradient descent method is applied in the LR algorithm to calculate the optimum weights. The radial basis function is used as the kernel in the SVM algorithm. The kernel parameters and penalty factors are optimized by the least square method.

### B. Diversity Measures of the Base Classifiers

The primary goal of EL is to improve the performance of a model by aggregating multiple weak classifiers. In EL, the diversity among base classifiers plays an essential role for constructing effective ensemble systems. Kuncheva *et al.* summarize 10 typical measures of diversity [31], among which the *Q* statistics is selected as the diversity measure in this work. The calculation method of *Q* statistics is expressed as follows: Assume that the number of the base classifiers is $L_c$; $C_i$ and $C_j$ ($i$, $j$=1, 2, ⋯⋯ , $L_c$, $i \neq j$) are two different base classifiers; $N^{11}$($N^{00}$) is the number of samples that $C_i$ and $C_j$ both classify correctly (incorrectly); $N^{10}$($N^{01}$) is the number of samples that meet the following requirements: $C_i$($C_j$) classifies them correctly and $C_j$($C_i$) misclassifies them. The relationship between a pair of classifiers is shown in Table Ⅱ, and the calculation of *Q* statistics can be expressed as:

$$Q_{ij} = \frac{N^{11}N^{00} - N^{01}N^{10}}{N^{11}N^{00} + N^{01}N^{10}}. \quad (1)$$

It can be seen from (1) that, if the two classifiers demonstrate the same classification results, i.e. $N^{10}$=$N^{01}$=0, then $Q$=1, and the diversity between these two classifiers is the lowest. Oppositely, if the two classifiers have different classification results on each sample, i.e. $N^{11}$=$N^{00}$=0, then $Q$= −1, in which the diversity is the highest. Furthermore, the diversity of the whole ensemble system can be calculated with

$$Q = \frac{2}{L_c(L_c-1)} \sum_{i=1}^{L_c-1} \sum_{j=i+1}^{L_c} Q_{ij}. \quad (2)$$

### C. Training and Testing of the Heterogeneous EL Model

A heterogeneous EL model is established by importing the Bagging strategy into MHLNN, *k*-NN (*k*=3), LR, and SVM. The Bagging algorithm is one of the representatives of the parallel EL method [32]. As illustrated in Fig. 10, the procedure of constructing an EL model with Bagging is that: Firstly, the Bootstrap method is utilized to randomly resample the samples in the dataset with replacement to attain multiple sub-datasets with same size. The probability $p$ of the samples not being selected in a sub-dataset can be expressed as

$$\begin{cases} p = \left(1 - \frac{1}{n}\right)^n \\ \lim_{n\to\infty} \left(1 - \frac{1}{n}\right)^n \approx 36.8\% \end{cases}, \quad (3)$$

where $n$ is the number of samples in the dataset. When $n$ tends to infinity, the limit value of $p$ is around 36.8%, and, accordingly, the probability of the samples being selected is 63.2% approximately. The selected samples, termed as in-bag (IB) data, are used to train the EL model, while the unselected samples, termed as out-of-bag (OOB) data, can be used as the validation data to estimate the accuracy and generalization of the EL model. Secondly, in this work, four sub-datasets are generated and used to train the base classifiers respectively. Lastly, the final classification result of the EL model can be determined by aggregating the outputs of all the base classifiers with the majority voting strategy.

In the majority voting strategy, the final classification is decided based on the agreement of more than half of the base classifiers. This EL model can be parallelized to accelerate the computation. This EL model is an open system, which can be further improved by integrating any other base classifiers, such as decision tree, deep belief network, and convolution residual network. Additionally, with aim to compare the classification performance between the EL model and the other data-driven models conveniently, the OOB data are also designed to account for 20% of all the samples in the dataset.

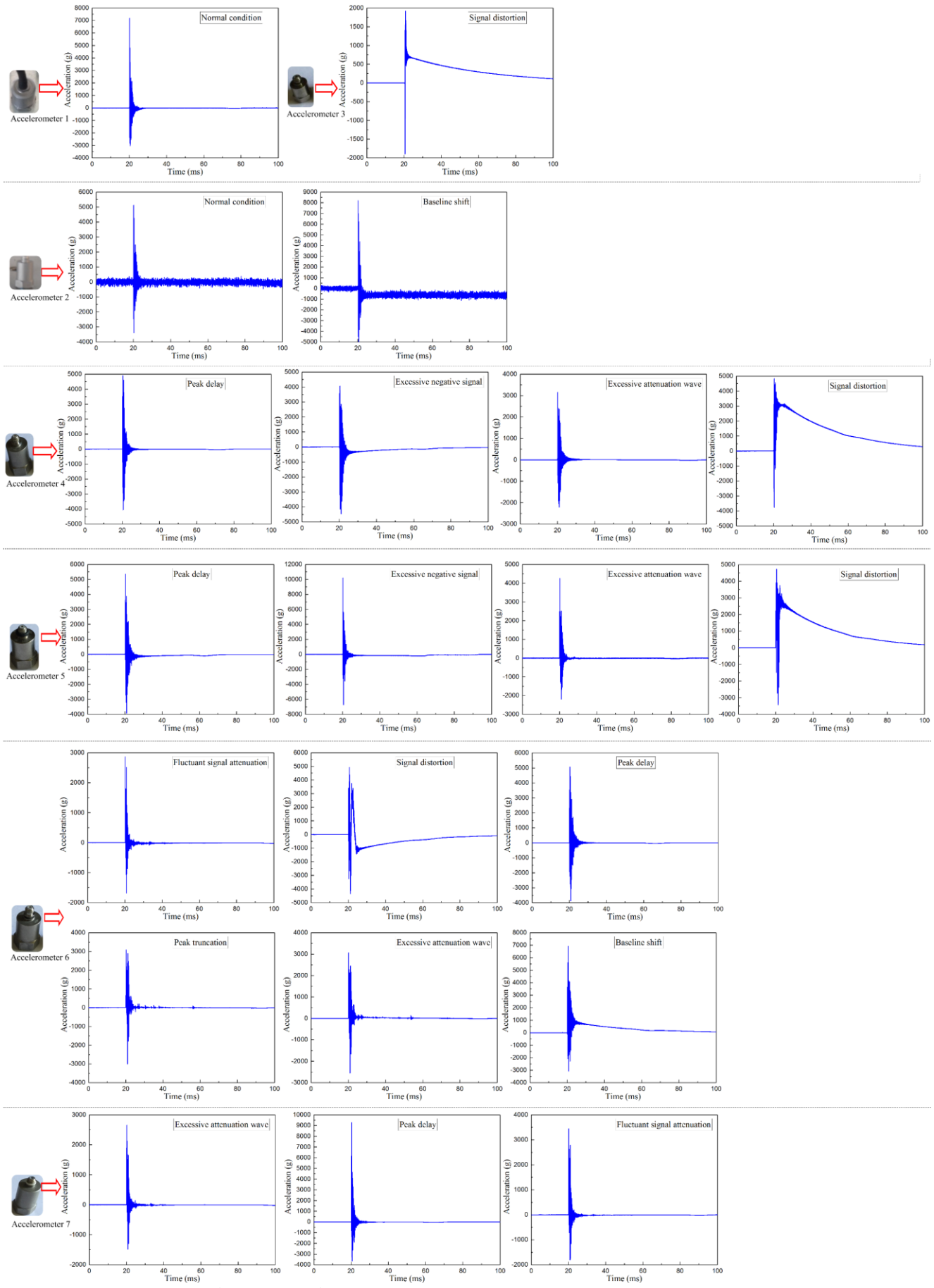


Fig. 7. The mutable shock signal waveforms measured from each accelerometer.

TABLE I.
THE SUMMARIZATION OF THE ACCELEROMETERS' HEALTH CONDITIONS.

| Accelerometer label | Fault types | Description of the readings | Number of samples |
|---|---|---|---|
| Accelerometer 1 | Type 1: no fault | Normal condition | 751 |
| Accelerometer 2 | Type 2: overstress of the sensitive element | Normal condition; Baseline shift | 510 |
| Accelerometer 3 | Type 3: damage of the sensitive element | Signal distortion | 510 |
| Accelerometer 4 | Type 4: mounting base loosening | Peak delay; Excessive negative signal; Excessive attenuation wave; Signal distortion | 510 |
| Accelerometer 5 | Type 5: sensitive element loosening | Excessive attenuation wave; Peak delay; Excessive negative signal; Signal distortion | 241 |
| Accelerometer 6 | Type 6: mass block loosening | Fluctuant signal attenuation; Peak delay Signal distortion; Peak truncation; Excessive attenuation wave; Baseline shift | 241 |
| Accelerometer 7 | Type 7: low resonant response | Excessive attenuation wave; Peak delay Fluctuant signal attenuation | 241 |

TABLE Ⅱ.
THE RELATIONSHIP BETWEEN A PAIR OF CLASSIFIERS.

| | $C_j$ correct | $C_j$ incorrect |
|---|---|---|
| $C_i$ correct | $N^{11}$ | $N^{10}$ |
| $C_i$ incorrect | $N^{01}$ | $N^{00}$ |

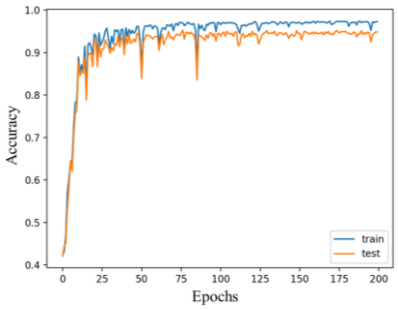


Fig. 8. Accuracy curve of the proposed MHLNN during training.

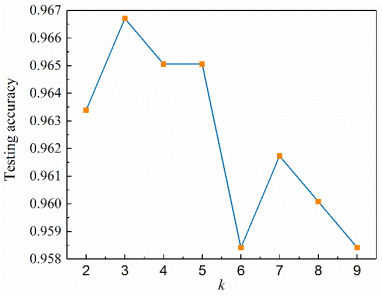


Fig. 9. Performance of *k*-NN algorithm with different *k*'s.

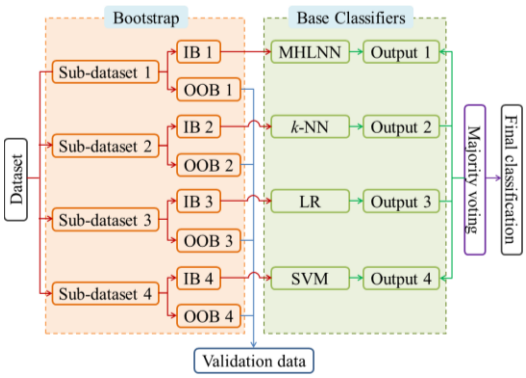


Fig. 10. Brief flowchart of constructing the heterogeneous EL model.

### D. Training and Testing of the Hybrid EL Model

It can be seen from Fig. 9 that the accuracy of the *k*-NN varies with different *k*'s. It is likely that the *k*-NN method with different *k*'s could figure out confusion matrices with different diversities. So, adding the classification results computed from *k*-NN with other *k*'s into the heterogeneous EL model would further improve the diagnosis performance. This hybrid EL model integrates not only heterogeneous models, including MHLNN, *k*-NN, LR, and SVM, but also homogeneous models, i.e. the *k*-NN with different *k*'s. Similarly, as shown in Fig. 11, the Bagging algorithm and the majority voting strategy are both adopted to construct this hybrid EL model.

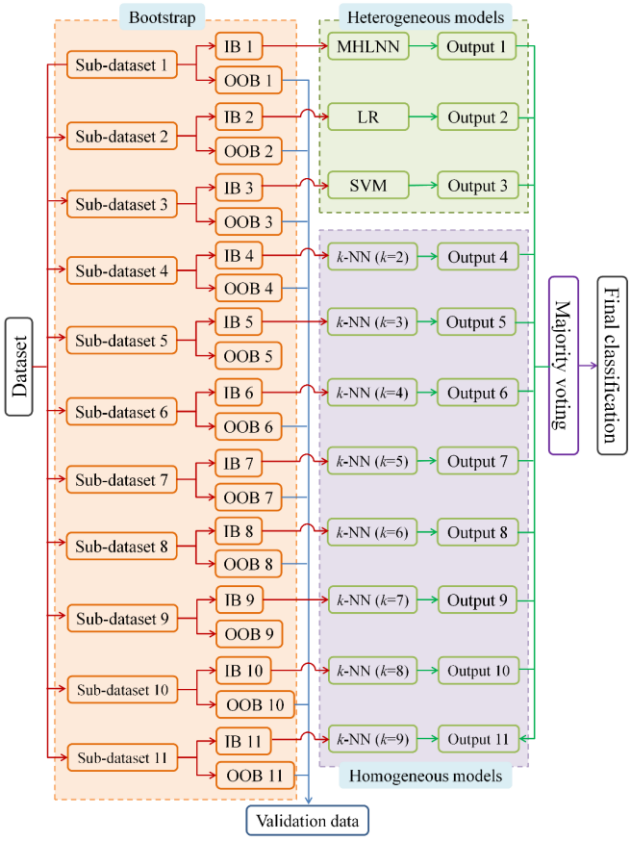


Fig. 11. Brief flowchart of constructing the hybrid EL model.

## V. EXPERIMENTAL RESULTS

### A. Visualization of the Proposed Data-driven Methods

In order to further estimate the experimental results, visualization analysis is conducted to give a more intuitive understanding for the proposed data-driven methods. The features of all the shock signals extracted by the proposed

MHLNN model are visualized with t-SNE technique, which is a nonlinear dimensionality reduction algorithm for visualizing high-dimensional data in good performance [33]. The final t-SNE output is visualized in Fig. 12, where different colors represent different fault types described in Table I.

To analyze the classification accuracy of each individual category, the confusion matrices of the proposed data-driven models are visualized in Fig. 13. It gives the correctly classified samples and misclassified samples for each fault type. The columns and rows represent the true labels and the predicted labels respectively. The diagonal blocks show the number of samples that are correctly classified. Setting the subscript serial number 1, 2, … , 11 to represent the MHLNN, *k*-NN (*k*=3), LR, SVM, *k*-NN (*k*=2), *k*-NN (*k*=4), *k*-NN (*k*=5), …, *k*-NN (*k*=9) methods respectively, the diversities between each two data-driven models are calculated with (1) and listed in Table Ⅲ. In this Table, $Q_{1,2}$ is the $Q$ statistics between the MHLNN and the *k*-NN (*k*=3); $Q_{1,3}$ is the $Q$ statistics between the MHLNN and the LR, and so on. The confusion matrix of the proposed heterogeneous EL model is visualized in Fig. 14. The confusion matrices of the *k*-NN with different *k*'s are shown in Fig. 15. Lastly, the confusion matrix of the proposed hybrid EL model is visualized in Fig. 16. According to (2), the calculated diversity of this hybrid EL system is 0.978.

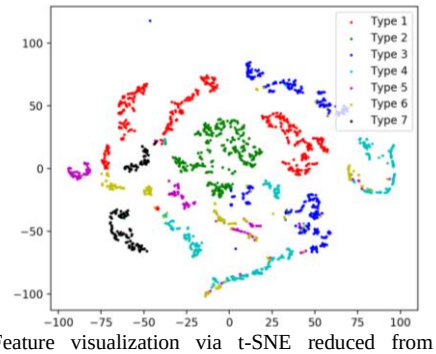


Fig. 12. Feature visualization via t-SNE reduced from the learned representations for the test dataset with the proposed MHLNN.

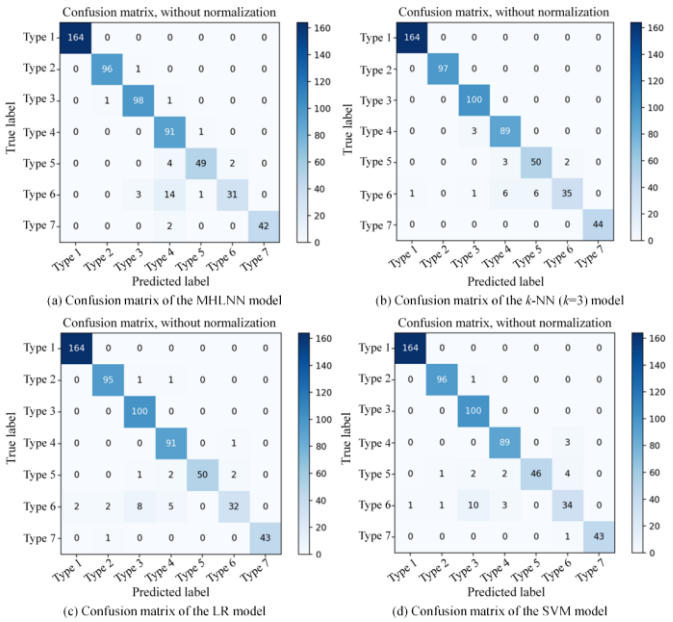


Fig. 13. Confusion matrices of the different base classifiers, including MHLNN, *k*-NN (*k*=3), LR, and SVM.

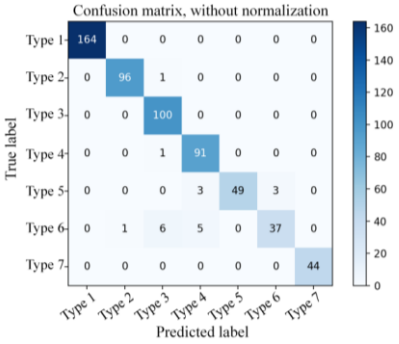


Fig. 14. Confusion matrix of the proposed heterogeneous EL model.

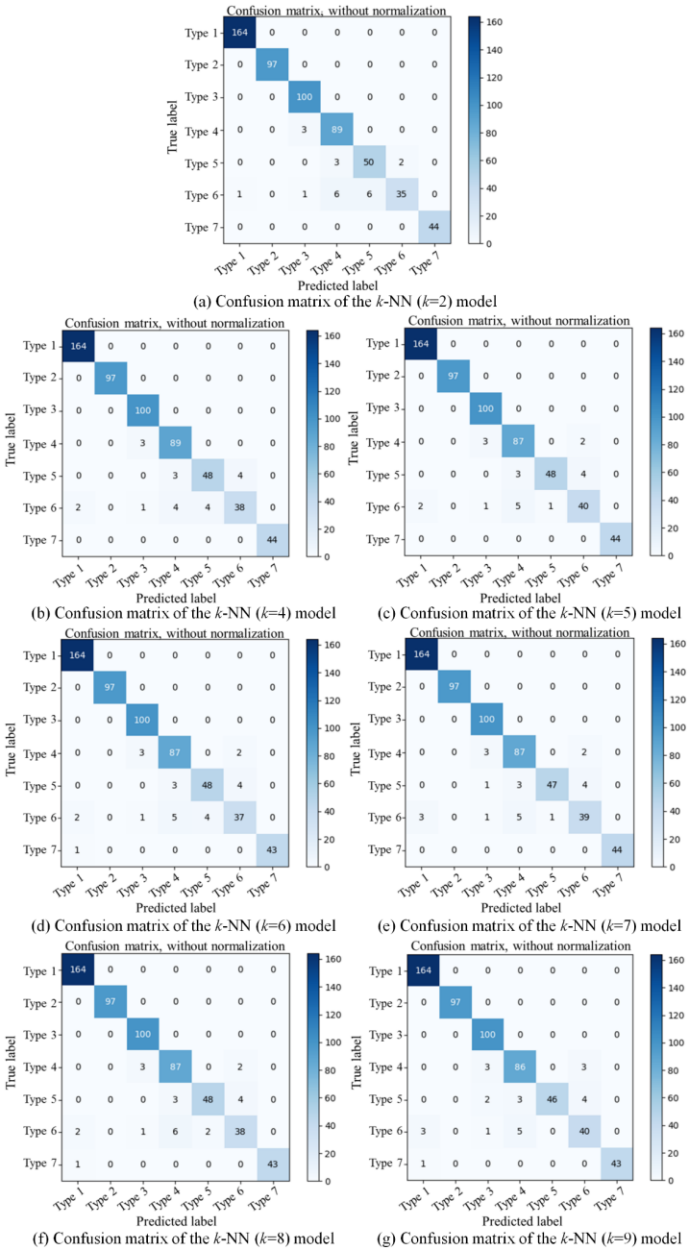


Fig. 15. Confusion matrices of the *k*-NN with different k's.

## *B. Quantification for the Diagnosis Performance*

In this work, four typical indicators, Accuracy (*A*), Precision (*P*), Recall (*R*), and $F_1$-score ($F_1$), are used to quantify the performance of all the data-driven models. These indicators are chosen because they can reflect the health monitoring

requirements directly and are widely adopted for performance evaluation and comparison of multiclass classification problems [34]. The calculation formulas for these indicators are shown in (4). Besides, the computation time ($T$) is also selected for the performance evaluation. Note that, because of the parallel computation nature in the EL, the computation time of the EL model depends on the most time-consuming base classifier.

$$\begin{cases} A = \dfrac{TP+TN}{TP+TN+FN+FP} \\ P = \dfrac{TP}{TP+FP} \\ R = \dfrac{TP}{TP+FN} \\ F_1 = \dfrac{2PR}{P+R} \end{cases} . \tag{4}$$

In (4), *TP* (True Positive) is the number of samples correctly classified in the positive category; *TN* (True Negative) is the number of samples correctly classified in the negative category; *FN* (False Negative) is the number of samples misclassified in the negative category; *FP* (False Positive) is the number of samples misclassified in the positive category. Among these indicators, *P* and *R* is a pair of contradictory metrics; $F_1$-score is the harmonic mean of *P* and *R*, which illustrates the classification performance of each category; *A* is the ratio of the correct number of samples to the total number of samples, which reflects the overall performance. Based on these indicators, the performance comparison of all the proposed data-driven models is shown in Table Ⅳ.

TABLE Ⅲ.
THE DIVERSITIES BETWEEN EACH TWO BASE CLASSIFIERS.

| | | | | | | | |
|---|---|---|---|---|---|---|---|
| | $Q_{1,2}$ | $Q_{1,3}$ | $Q_{1,4}$ | $Q_{1,5}$ | $Q_{1,6}$ | $Q_{1,7}$ | $Q_{1,8}$ |
| $Q$ statistic | 0.968 | 0.976 | 0.960 | 0.959 | 0.964 | 0.964 | 0.956 |
| | $Q_{1,9}$ | $Q_{1,10}$ | $Q_{1,11}$ | $Q_{2,3}$ | $Q_{2,4}$ | $Q_{2,5}$ | $Q_{2,6}$ |
| $Q$ statistic | 0.954 | 0.960 | 0.956 | 0.945 | 0.949 | 0.997 | 0.999 |
| | $Q_{2,7}$ | $Q_{2,8}$ | $Q_{2,9}$ | $Q_{2,10}$ | $Q_{2,11}$ | $Q_{3,4}$ | $Q_{3,5}$ |
| $Q$ statistic | 0.999 | 0.999 | 0.998 | 0.998 | 0.997 | 0.996 | 0.9761 |
| | $Q_{3,6}$ | $Q_{3,7}$ | $Q_{3,8}$ | $Q_{3,9}$ | $Q_{3,10}$ | $Q_{3,11}$ | $Q_{4,5}$ |
| $Q$ statistic | 0.953 | 0.939 | 0.967 | 0.956 | 0.962 | 0.934 | 0.961 |
| | $Q_{4,6}$ | $Q_{4,7}$ | $Q_{4,8}$ | $Q_{4,9}$ | $Q_{4,10}$ | $Q_{4,11}$ | $Q_{5,6}$ |
| $Q$ statistic | 0.956 | 0.943 | 0.974 | 0.957 | 0.971 | 0.959 | 0.998 |
| | $Q_{5,7}$ | $Q_{5,8}$ | $Q_{5,9}$ | $Q_{5,10}$ | $Q_{5,11}$ | $Q_{6,7}$ | $Q_{6,8}$ |
| $Q$ statistic | 0.990 | 0.992 | 0.991 | 0.990 | 0.988 | 0.997 | 0.998 |
| | $Q_{6,9}$ | $Q_{6,10}$ | $Q_{6,11}$ | $Q_{7,8}$ | $Q_{7,9}$ | $Q_{7,10}$ | $Q_{7,11}$ |
| $Q$ statistic | 0.995 | 0.994 | 0.993 | 0.999 | 0.999 | 0.999 | 0.999 |
| | $Q_{8,9}$ | $Q_{8,10}$ | $Q_{8,11}$ | $Q_{9,10}$ | $Q_{9,11}$ | $Q_{10,11}$ | $Q$ |
| $Q$ statistic | 0.999 | 0.999 | 0.997 | 0.999 | 0.999 | 0.999 | 0.979 |

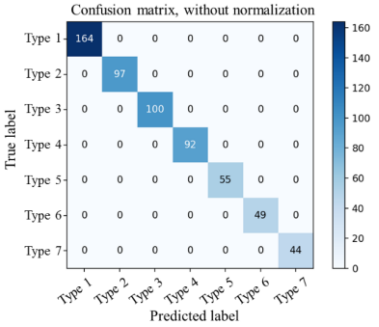


Fig. 16. Confusion matrix of the proposed hybrid EL model.

TABLE Ⅳ.
PERFORMANCE COMPARISON OF DIFFERENT DATA-DRIVEN MODELS IN PREDICTING THE TESTING DATA (CORE I5, 2.3GHZ).

| Indicators | MHLNN | *k*-NN (*k*=2) | *k*-NN (*k*=3) | *k*-NN (*k*=4) | *k*-NN (*k*=5) | *k*-NN (*k*=6) | *k*-NN (*k*=7) | *k*-NN (*k*=8) | *k*-NN (*k*=9) | LR | SVM | Heterogeneous EL | Hybrid EL |
|---|---|---|---|---|---|---|---|---|---|---|---|---|---|
| *A* (%) | 95.0 | 96.3 | 96.3 | 96.5 | 96.5 | 95.8 | 96.2 | 96.0 | 95.8 | 95.7 | 95.1 | 96.7 | 100 |
| *P* (%) | 92.0 | 95.8 | 94.2 | 95.8 | 95.9 | 94.9 | 95.7 | 95.3 | 95.5 | 93.0 | 92.4 | 94.7 | 100 |
| *R* (%) | 95.2 | 94.2 | 95.7 | 94.5 | 94.8 | 93.6 | 94.2 | 93.9 | 93.8 | 95.7 | 94.5 | 96.6 | 100 |
| $F_1$ (%) | 93.0 | 94.7 | 94.7 | 95.1 | 95.3 | 94.2 | 94.9 | 94.5 | 94.5 | 93.9 | 93.2 | 95.4 | 100 |
| *T* (ms) | 3.3 | 1494 | 1912 | 1627 | 1714 | 1643 | 1642 | 1653 | 1765 | 7 | 11 | - | - |

## VI. DISCUSSION

It can be seen from Fig. 12 that the features of different fault types are separable by the proposed MHLNN, which means that the MHLNN model is able to extract meaningful features and cluster the learned features effectively.

It can be found from Fig. 13 that though few samples are misclassified, majority of samples fall on the diagonal blocks of the confusion matrices, which demonstrates the good diagnosis performance of all the data-driven models. Meanwhile, through comparing the outliers in Fig. 13 (a)-(d), it is found that, for each fault type, more samples are misclassified with MHLNN, but fewer misclassification with *k*-NN (*k*=3), meaning that the *k*-NN model with *k*=3 has the best performance among all the investigated data-driven models. Additionally, a phenomenon observed from Fig. 13 is that the major misclassified samples are focused on the type 6. This phenomenon is in accordance with the observation in Fig. 7 and Table I, where the shock signals measured from accelerometer 6 demonstrate similar characteristics with the other accelerometers.

By comparing the confusion matrices in Fig. 13 and Fig. 14, it can be found that, in Fig. 14, majority of the samples land on the diagonal blocks of the confusion matrix, and fewer samples misclassified by the proposed heterogeneous EL model, which means that the EL model has higher diagnosis performance than each single classifier. Similarly, the main misclassified samples are contributed by accelerometer 6, but alleviated by the EL method to some extent, which illustrates the superiority of the proposed EL model indirectly.

As demonstrated in Fig. 15, it can be seen that the *k*-NN model with different *k*'s does generate different classification results, demonstrating the diversity among these base classifiers. Subsequently, as shown in Table Ⅲ, the *Q* statistics between each two base classifiers effectively quantify the diversities among all the base classifiers, which illustrate potentials to further improve the diagnosis accuracy by aggregating these *k*-NN-based classifiers with the EL method.

As shown in Fig. 16, it can be found that all the samples are correctly classified on the diagonal blocks. This excellent classification result directly illustrates the effectiveness and high-performance of the proposed hybrid EL method.

As shown in Table Ⅳ, the diagnosis performance of all the proposed data-driven methods are quantified with four indicators, including accuracy, precision, recall, and $F_1$-score. Overall, all the proposed data-driven models have achieved good results in all the four indicators: all above 92%, which demonstrates that the classical data-driven methods can be used to solve the fault diagnosis problems of high-accelerometers to some extent. From the details in Table Ⅳ, it can be concluded that the proposed EL model has best diagnosis performance in all the four indicators than the other base classifiers, which also verifies the advantage of EL method in addressing fault classification problems. Especially, for the hybrid EL model, the diagnosis performance is improved significantly by further integrating the *k*-NN models with other *k*'s. Besides, it can be found from Table Ⅳ that the *k*-NN-based method has lower computation efficiency than other base classifiers, which also drags on the computation efficiency of the EL method. Actually, low computation efficiency is one of the inherent drawbacks of the EL method, but, fortunately, it is affordable in this work.

## VII. Conclusions and Further Research

In this work, an open question, that there is no comprehensive research in using data-driven methods to diagnose the fault types of high-g accelerometers, is proposed for the first time. To fill this gap, an experimental setup, which consists of a high-g shock test system and six accelerometers with different fault types, is firstly designed to produce shock signal dataset. All the experimental setup is consistent with the real-world shock test practice, and, thus, the collected dataset can reflect the working conditions of high-g accelerometers under real shock tests, which are different than the datasets simulated from laboratory machines in most traditional fault diagnosis fields. Then, five data-driven approaches are proposed to identify the fault types of high-g accelerometers by being benchmarked on the collected dataset. These data-driven methods include MHLNN, *k*-NN, LR, SVM, and EL, in which the EL model is constructed with the Bagging strategy by integrating the other four data-driven models as the base classifiers. Lastly, all the classification results are calculated and depicted with various visualization methods and quantification indicators. The final diagnosis results illustrate that the data-driven methods can be applied to deal with the fault diagnosis problem of high-g accelerometers in shock test field with high potentials. Again, the proposed hybrid EL model shows better diagnosis performance than all the base classifiers, and also verifies that the EL methodology can effectively compensate the classification results of each individual classifier by utilizing the diversity and tends to enhance the identification accuracy over these individuals.

This work is the first attempt to introduce the data-driven methods into the fault diagnosis of high-g accelerometers in shock test field. In the future work, a valuable point worth further investigation is that the operation faults and other setup faults should be allowed for instead of merely concerning the faults of accelerometer itself.

## References

[1] A. García-Pérez, F. Sorribes-Palmer, G. Alonso, and A. Ravanbakhsh, "Overview and application of FEM methods for shock analysis in space instruments," *Aerosp. Sci. Technol.*, vol. 80, pp. 572-586, Sep., 2018.

[2] X. Wang, Z. Qin, J. Ding, and F. Chu, "Finite element modeling and pyroshock response analysis of separation nuts," *Aerosp. Sci. Technol.*, vol. 68, pp. 380-390, Sep., 2017.

[3] S. Ryan, S. Thaler, S. Kandanaarachchi, "Machine learning methods for predicting the outcome of hypervelocity impact events," *Expert Syst. Appl.*, vol. 45, no. 1, pp. 23-39, Mar. 2016.

[4] Z. Zhang, L. Li, and D. Zhang. Effect of arbitrary yaw/pitch angle in bird strike numerical simulation using SPH method. *Aerosp. Sci. Technol.*, vol. 81, pp. 284-293, Oct., 2018.

[5] J. Wen, C. Liu, H. Yao, and B. Wu, "A nonlinear dynamic model and parameters identification method for predicting the shock pulse of rubber waveform generator," *Int. J. Impact. Eng.*, vol. 120, pp. 1-15, Oct., 2018.

[6] B. Wu, C. Liu, and J. Wen, "The optimized algorithm for working parameters of the vertical impact testing machine," in *Proc. ICEMI*, Yangzhou, China, 2017, pp. 424-430.

[7] J. Wen, H. Yao, B. Wu, Y. Ren, and Z. Ji, "A Deep Learning Approach to Recover High-g Shock Signals from the Faulty Accelerometer," *IEEE Sens. J.*, vol. 20, no. 4, pp. 1761-1769, Feb., 2019.

[8] H. Yao, J. Wen, Y. Ren, B. Wu, and Z. Ji, "Low-cost measurement of industrial shock signals via deep learning calibration," in *Proc. ICASSP*, Brighton, UK, 2019, pp. 2892-2896.

[9] J. Liu, Y. Shi, P. Li, J. Tang, R. Zhao, and H. Zhang, "Experimental study on the package of high-g accelerometer," *Sensor. Actuat. A-Phys.*, vol. 173, no. 1, pp. 1-8, Jan., 2012.

[10] J. A. Walraven, "Failure analysis issues in microelectromechanical systems (MEMS)," *Microelectron. Reliab.*, vol. 45, no. 9-11, pp. 1750-1757, Sep.-Nov., 2005.

[11] Y. P. Zhao, and T. X. Yu, "Failure modes of MEMS and microscale adhesive contact theory," *Int. J. Nonlin. Sci. Num.*, vol. 1(Supplement), pp. 361-372, Dec., 2000.

[12] W. Xia, S. Fan, W. Xing, T. Ma, J. Zu, and J. Fan, "Restraining zero drift in an ultrahigh-g impact environment," *Meas. Sci. Technol.*, vol. 23, no.3, pp. 035108, Feb., 2012.

[13] L. A. Escobar, and W. Q. Meeker, "A review of accelerated test models," *Stat. Sci.*, vol. 21, no.4, pp. 552-577, Nov., 2006.

[14] A. Izadian, P. Khayyer, and P. Famouri, "Fault diagnosis of time-varying parameter systems with application in MEMS LCRs," *IEEE T. Ind. Electron.*, vol. 56, no. 4, pp. 973-978, Apr., 2008.

[15] K. Worden, W. J. Staszewski, and J. J. Hensman, "Natural computing for mechanical systems research: A tutorial overview," *Mech. Syst. Signal. Pr.*, vol. 25, no.1, pp. 4-111, Jan., 2011.

[16] L. Zhang, J. Lin, B. Liu, Z. Zhang, X. Yan and M. Wei, "A Review on Deep Learning Applications in Prognostics and Health Management," *IEEE Access*, vol. 7, pp. 162415-162438, Nov., 2019.

[17] H. Shao, H. Jiang, H. Zhao, and F. Wang, "A novel deep autoencoder feature learning method for rotating machinery fault diagnosis," *Mech. Syst. Signal. Pr.*, vol. 95, pp. 187-204, Oct., 2017.

[18] Y. Zhou, M. Huang, Y. Chen, and Y. Tao, "A novel health indicator for on-line lithium-ion batteries remaining useful life prediction," *J. Power Sources*, vol. 321, no. 30, pp. 1-10, Jul., 2016.

[19] Y. Ling, and S. Mahadevan, "Integration of structural health monitoring and fatigue damage prognosis," *Mech. Syst. Signal. Pr.*, vol. 28, pp. 89-104, Apr., 2012.

[20] A. Zhang, "High acceleration board level reliability drop test using dual mass shock amplifier," in *Proc. ECTC*, Orlando, FL, USA, 2014, pp. 1441-1448.

[21] L. Guo, Y. Lei, S. Xing, T. Yan, and N. Li, "Deep convolutional transfer learning network: A new method for intelligent fault diagnosis of machines with unlabeled data," *IEEE T. Ind. Electron.*, vol. 66, no. 9, pp. 7316-7325, Sep., 2019.

[22] M. Mohri, A. Rostamizadeh, and A. Talwalkar, "Foundations of machine learning," *MIT press*, 2018.

[23] Y. Li, and Y. Yuan, "Convergence analysis of two-layer neural networks with ReLU activation," in *Proc. NIPS*, Long Beach, CA, USA, 2017, pp. 597-607.

[24] C. Cortes, and V. Vapnik, "Support-vector networks," *Mach. Learn.*, vol. 20, no.3, pp. 273-297, Sep., 1995.

[25] S. Ma, and F. Chu, "Ensemble deep learning-based fault diagnosis of rotor bearing systems," *Comput. Ind.*, vol. 105, pp. 143-152, Feb., 2019.

[26] M. Amozegar, and K. Khorasani, "An ensemble of dynamic neural network identifiers for fault detection and isolation of gas turbine engines," *Neural Networks*, vol. 76, pp. 106-121, Apr., 2016.

[27] Z. Chen *et al.*, "Random forest based intelligent fault diagnosis for PV arrays using array voltage and string currents," *Energ. Convers. Manage.*,

vol. 178, no. 15, pp. 250-264, Dec., 2018.
[28] G. Jiang, H. He, J. Yan, and P. Xie, "Multiscale convolutional neural networks for fault diagnosis of wind turbine gearbox," *IEEE Trans. Ind. Electron.*, vol. 66, no. 4, pp. 3196-3207, Apr. 2019.
[29] W. Lu, B. Liang, Y. Cheng, D. Meng, J. Yang, and T. Zhang, "Deep model based domain adaptation for fault diagnosis," *IEEE Trans. Ind. Electron.*, vol. 64, no. 3, pp. 2296-2305, Mar., 2017.
[30] V. Narasimhan, H. Li, & M. Jianmin, "Micromachined high-g accelerometers: a review," *J. Micromech. Microeng.*, vol. 25, no. 3, pp. 033001, 2015.
[31] L. I. Kuncheva, & C. J. Whitaker, "Measures of diversity in classifier ensembles and their relationship with the ensemble accuracy," *Mach. Learn.*, vol. 51, no. 2, pp. 181-207, 2003.
[32] L. Breiman, "Bagging predictors," *Mach. Learn.*, vol. 24, no. 2, pp. 123-140, Aug., 1996.
[33] L. V. D. Maaten, and G. Hinton, "Visualizing data using t-SNE," *J Mach Learn Res*, vol. 9, pp. 2579-2605, Nov., 2008.
[34] J. Jiao, M. Zhao, J. Lin, and C. Ding, "Deep Coupled Dense Convolutional Network with Complementary Data for Intelligent Fault Diagnosis," *IEEE Trans. Ind. Electron.*, vol. 66, no. 12, pp. 9858-9867, Dec., 2019.

**Jingjing Wen** received the B.Eng. and M.Sc. degrees from the School of Astronautics, Northwestern Polytechnical University, Xi'an, China, in 2013 and 2016, respectively. He is currently pursuing the Ph.D. degree with Northwestern Polytechnical University. Since July 2019, he has been a Research Associate with Cardiff University, U.K. His main research interests include shock test, computer vision, machine learning, intelligent testing instrumentation, and aerospace engineering.

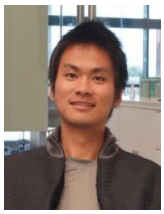

**Houpu Yao (GS'15)** is with JD Finance America Corporation. He received the bachelor's degree from Northwestern Polytechnical University, Xi'an, China, in 2013, and the Ph.D. degree in aerospace engineering from Arizona State University, Tempe, AZ, USA, in 2019. His research interests include computational mechanics and acoustics, deep learning and computer vision, parallel computation, material design, and autonomous driving.

**Ze Ji (M'19)** is a senior lecturer (associate professor) at the School of Engineering, Cardiff University, UK. He received his BEng (2001) from Jilin University, China, MSc (2003) from the University of Birmingham, UK, and PhD (2007) from Cardiff University, UK. Prior to his current position, he was working in industry on autonomous robotics. His research interests are cross-disciplinary, with a focus on autonomous robot navigation, computer vision, simultaneous localization and mapping (SLAM), machine learning, unmanned surface vehicles, and acoustic localization.

**Bin Wu** received his B.S. degree and M.Sc. degree from School of Astronautics, Northwestern Polytechnical University, Xi'an, China, in 1987 and 1998 respectively. Currently, he is an associated professor in Northwestern Polytechnical University. So far, he has more than 50 papers published and held more than 10 national patents. His main research interests include mass property measurement technique, test technology of mechanical environment, and aerospace engineering.

**Min Xia (GS'11-M'17)** received the B.S. degree from Southeast University, Nanjing, China, in 2009, the M.S. degree from the University of Science and Technology of China, Hefei, China, in 2012, and the Ph.D. degree from the University of British Columbia, Vancouver, Canada, in 2017. He is currently a Lecturer with the Department of Engineering at Lancaster University, Lancaster, Uk and adjunct research fellow at the Yangtze River Delta Research Institute of Northwestern Polytechnical University, Taicang, China. His research interests include smart manufacturing, machine diagnosis and prognosis, deep neutral networks, autonomous vehicle, and sensor fusion.